

# High-efficiency visible-light-driven oxidation of primary C–H bonds in toluene over CsPbBr<sub>3</sub> perovskite supported by hierarchical TiO<sub>2</sub> nanoflakes†

Received 00th January 20xx,  
Accepted 00th January 20xx

DOI: 10.1039/x0xx00000x

Jiayu Yi,<sup>a</sup> Sunzai Ke,<sup>a</sup> Suwei Lu,<sup>a</sup> Bo Weng,<sup>b</sup> Lijuan Shen,<sup>a</sup> Xuhui Yang,<sup>a</sup> Hun Xue,<sup>a</sup> Min-Quan Yang<sup>\*a</sup> and Qingrong Qian<sup>\*a</sup>

Photocatalytic oxidation of toluene to valuable fine chemicals is of great significance, yet challenged in the development of advanced catalysts with both high activity and selectivity for the activation of inert C(sp<sup>3</sup>)–H bonds. Halide perovskites with remarkable optoelectronic properties have shown to be prospective photoactive materials, but the bulky structure with small surface area and severe recombination of photogenerated electron-hole pairs are obstacles to application. Here, we fabricate a hierarchical nanoflower-shaped CsPbBr<sub>3</sub>/TiO<sub>2</sub> heterojunction by assembling CsPbBr<sub>3</sub> nanoparticles on 2D TiO<sub>2</sub> nanoflakes subunits. The design significantly downsizes the size of CsPbBr<sub>3</sub> from micrometer to nanometer, and forms type II heterojunction with intimate interfacial contact between the CsPbBr<sub>3</sub> and the TiO<sub>2</sub> nanoflakes, thereby accelerating the separation and transfer of photogenerated charges. Moreover, the formed hierarchical heterojunction heightens light absorption by the refraction and scattering, offers large surface area and enhances the adsorption of toluene molecules. Consequently, the optimized CsPbBr<sub>3</sub>/TiO<sub>2</sub> exhibits a high performance (10200 μmol g<sup>-1</sup> h<sup>-1</sup>) for photocatalytic toluene oxidation with high selectivity (85%) for benzaldehyde generation under visible light. The photoactivity is about 20 times higher than blank CsPbBr<sub>3</sub>, and is among the best photocatalytic performance reported for selective oxidation of toluene under visible light irradiation.

## Introduction

The direct oxidation of toluene to high-added-value fine chemicals, such as alcohols and aldehydes, is one of the most important conversions in chemical industry.<sup>1–4</sup> However, due to the inertness and high bond dissociation energy (89.8 kcal mol<sup>-1</sup>) of the C(sp<sup>3</sup>)–H bond,<sup>5</sup> the activation of toluene generally need to be operated under harsh reaction conditions (high pressure and temperature) and with the assistance of specific metal complexes or aggressive oxidants, which is expensive, energy intensive and causes negative impacts on the environment.<sup>6–8</sup> Solar-driven photocatalytic aerobic oxidation using molecular O<sub>2</sub> as oxidant represents a promising methodology to overcome these challenges, but the overall photocatalytic performance reported so far is still unsatisfactory due to the lack of desired photocatalysts with broad optical absorption windows, efficient charge separation, and high product selectivity.<sup>9–11</sup>

Over the past years, halide perovskite materials have triggered wide attention in photocatalysis because of their outstanding optical and electronic properties.<sup>12–16</sup> The high charge carrier mobility, visible light absorption, and tunable

band structures enable them to be potential competitors for photocatalytic oxidation of toluene.<sup>17,18</sup> Nevertheless, single-component halide perovskites typically evolve to bulky aggregates with large particle size (several to tens micrometers), which leads to severe bulk recombination of charge carriers and restricts the photoactivity.<sup>19,20</sup> To tackle the problem, construction of heterojunction is an effective strategy. By hybridization of the halide perovskite with preferred substrates, it not only can prevent the aggregation of the halide perovskites to mediate the bulk recombination of photoexcited electron–hole pairs, but also can establish interfacial built-in electric field to further facilitate the spatial charge transfer and separation.<sup>21</sup>

Moreover, the catalytic functions of photocatalysts also strongly depend on the nanostructure.<sup>22,23</sup> To realize high photocatalytic performance, the delicate design of well-defined nanostructure for heterojunction composites is also critical.<sup>24–27</sup> For diverse structural configurations, 3D hierarchical flower-like nanostructure constructed by 2D nanoflakes subunits have demonstrated intrinsic advantages for photocatalysis. Such hierarchical structure can strengthen the light absorption of photocatalysts by multi-light reflection and scattering within the nanoflakes subunits, and prohibit the aggregation of the 2D nanoflakes to afford large surface area with abundant active sites.<sup>28,29</sup> In addition, the nanoflakes subunits will greatly shorten the diffusion path of charges, thereby facilitating the separation and transfer of photogenerated charges to surface for redox reactions.<sup>30,31</sup> Thus, the development of advanced 2D subunits-assembled hierarchical structure with heterogeneous junction would be promising for high-efficiency photocatalytic toluene oxidation.

Here, inspired by these above considerations, we design and fabricate a hierarchical nanoflower-shaped CsPbBr<sub>3</sub>/TiO<sub>2</sub>

<sup>a</sup> College of Environmental and Resource Sciences, College of Carbon Neutral Modern Industry, Fujian Key Laboratory of Pollution Control & Resource Reuse, Fujian Normal University, Fuzhou 350117, P.R. China

<sup>b</sup> cMACS, Department of Microbial and Molecular Systems, KU Leuven, Celestijnenlaan 200F, 3001 Leuven, Belgium

Electronic Supplementary Information (ESI) available: [details of any supplementary information available should be included here]. See DOI: 10.1039/x0xx00000x

(abbreviated as CPB/TiO<sub>2</sub>) heterojunction composed of TiO<sub>2</sub> nanoflakes-supported all-inorganic CsPbBr<sub>3</sub> perovskite nanoparticles. Benefiting from the composition and nanostructure engineering, the CPB/TiO<sub>2</sub> heterojunction displays excellent performance for photocatalytic toluene oxidation under the irradiation of visible light. The optimized 20%CPB/TiO<sub>2</sub> heterojunction composite delivers a toluene conversion rate of 10200 μmol g<sup>-1</sup> h<sup>-1</sup> and a high selectivity of 85% towards benzaldehyde (benzyl alcohol as the main by-product). The performance outperforms most of the state-of-the-art catalysts in literature for visible-light-driven oxidation of toluene. This work provides a new idea by constructing hierarchical heterojunction structure over halide perovskite materials for high-efficiency photocatalytic toluene conversion.

## Experimental section

### Materials

Cesium bromide (CsBr, 99.999%), lead bromide (PbBr<sub>2</sub>, 99.0%) and tetrahydrofuran (THF), were purchased from Macklin (Shanghai, China). N, N-Dimethylformamide (DMF), toluene, tetrabutyl titanate (TBOT), ethanol (EtOH), concentrated hydrochloric acid (HCl, 36%), acetic acid and glycerol were obtained from Sinopharm Chemical Reagent Co., Ltd. (Shanghai, China). All chemicals and solvents were used without further purification.

### Synthesis of mesoporous hierarchical TiO<sub>2</sub> nanoflowers

Typically, 1.5 g of Pluronic F127 was dispersed into a mixed solvent of 2.4 mL acetic acid, 3.2 mL concentrated hydrochloric acid (HCl) and 30 mL tetrahydrofuran (THF). After vigorously stirring for 20 min, 3.4 mL tetrabutyl titanate (TBOT) and 0.2 mL H<sub>2</sub>O were added subsequently to obtain a clear primrose yellow solution. After that, the solution was dried in an oven at 45 °C for 24 h to form a light-yellow gel. Then, 1.0 g of the gel was added into 25 mL ethanol (EtOH) and 5 mL glycerin under vigorous stirring. After 20 min, the transparent solution was transferred to a 50 mL Teflon-lined autoclave, heated at 150 °C for 15 h, and then cooled naturally to room temperature. The precipitation was washed with ethanol, and dried at 60 °C in oven.<sup>32</sup> Finally, the precipitation was calcinated in a Muffle furnace at 400 °C for 5 h with a heating rate of 1 °C min<sup>-1</sup> to obtain the hierarchical TiO<sub>2</sub> nanoflowers. To synthesize the collapsed TiO<sub>2</sub> without hierarchical nanoflower structure, the precipitation was calcinated in the same Muffle furnace at 400 °C for 5 h, but with a heating rate of 5 °C min<sup>-1</sup>.

### Synthesis of CsPbBr<sub>3</sub>/TiO<sub>2</sub> composites and blank CsPbBr<sub>3</sub>

CsPbBr<sub>3</sub>/TiO<sub>2</sub> composites were synthesized according to an antisolvent precipitation method at room temperature.<sup>33</sup> Typically, 1 mmol CsBr and 1 mmol PbBr<sub>2</sub> were dissolved in 10 mL of N, N-Dimethylformamide (DMF) by ultrasonication to form a precursor solution. Meanwhile, 100 mg TiO<sub>2</sub> was dispersed into 10 mL of DMF and stirred to form a uniform white dispersion. Then a certain amount of the CsPbBr<sub>3</sub> precursor

solution was added into the TiO<sub>2</sub> dispersion under ultrasonication. Then, the mixture was added dropwise into 50 ml toluene and stirred vigorously for 30 min. After that, the solution was centrifuged at 8000 rpm for 3 min. The precipitation was collected and dried in a vacuum oven. The series of x% CsPbBr<sub>3</sub>/TiO<sub>2</sub> composites were synthesized by changing the volume of the added CsPbBr<sub>3</sub> precursor solution, where x is the mass ratio of CsPbBr<sub>3</sub> in the composite (x = 10, 20, 30, 40). Blank CsPbBr<sub>3</sub> was prepared by the same procedure without the addition of TiO<sub>2</sub>.

### Characterizations

Scanning electron microscopy (SEM) images were captured by Hitachi 8100. Transmission electron microscopy (TEM) and high-resolution transmission electron microscopy (HRTEM) images were recorded using a JEM-2100F EX microscope at an accelerating voltage of 200 kV. The Brunauer-Emmett-Teller (BET) specific surface area was measured by N<sub>2</sub> adsorption-desorption instrument (BELSORP-mini II). The X-ray diffraction (XRD) patterns of the catalysts were characterized on a Bruker D8 advance X-ray diffractometer operated at 40 kV and 40 mA with a Cu Kα radiation in the 2θ ranging from 10° to 80°. The UV-Vis diffuse reflectance spectra (DRS) were obtained on a CARY-100 spectrophotometer (Agilent) using 100% BaSO<sub>4</sub> powder as a standard sample. X-ray photoelectron spectroscopy (XPS) was recorded by an X-ray photoelectron spectrometer (Thermo Escalab 250 electron spectrometer) with Al-Kα radiation. Raman spectra were obtained using a laser at a wavelength of 785 nm (Thermo Fisher Scientific, DXR 2xi). Photoluminescence (PL) spectra of solid samples were obtained by an RF-5301PC spectrophotometer (Shimadzu, Japan) with the 435 nm excitation wavelength.

Electron paramagnetic resonance (EPR) measurements were performed at room temperature using a Magnetech ESR5000X spectrometer. In general, 10 mg samples were dispersed in a mixed solution of 2 mL CH<sub>3</sub>CN containing 1 mL toluene and 2 μL 5,5-dimethyl-1-pyrroline-N-oxide (DMPO). The suspension was then transferred into a glass capillary. The sealed glass tube was then placed in the microwave cavity of the EPR spectrometer and exposed to a 300 W Xe lamp source (CEL-PF300-T8, Beijing China Education Au-light Co., Ltd.) at room temperature.

### Photoelectrochemical measurements

The photoelectrochemical analysis was carried out in a conventional three-electrode cell using a Pt plate and an Ag/AgCl electrode as the counter electrode and the reference electrode, respectively. The working electrode was prepared on fluorine-doped tin oxide (FTO) glass that was cleaned by ultrasonication in ethanol for 1 h. Typically, 5 mg of the catalyst was dispersed in 0.5 mL of isopropanol to get a slurry. After that, 20 μL of the slurry was dropped onto FTO with a size of 1 cm<sup>2</sup> and dried in air. The electrochemical impedance spectroscopy (EIS) measurement was performed in an electrolyte of tetrabutylammonium hexafluorophosphate (TBAPF<sub>6</sub>) in ethyl acetate (EA). Transient photocurrent was tested in the same electrolyte and a 300 W Xe lamp (CEL-PF300-T8, Beijing China

Education Au-light Co., Ltd.) equipped with a 420 nm cutoff filter ( $\lambda \geq 420$  nm) is used as light source. Mott-schottky measurement was performed in an electrolyte of 0.1 M TBAPF<sub>6</sub> in CH<sub>2</sub>Cl<sub>2</sub>.

### Density functional theory (DFT) calculations

DFT calculations were carried out using the Vienna ab initio simulation package (VASP) with the projector-augmented-wave (PAW) method.<sup>34</sup> The Perdew-Burke-Ernzerhof (PBE) scheme was used for the exchange correlation function, employing the generalized gradient approximation (GGA).<sup>35</sup> The electronic wave function was expanded using a plane wave basis with an energy cutoff of 500 eV. The energy convergence criterion was set to  $1.0 \times 10^{-5}$  eV, and the force convergence criterion was set to  $0.03$  eV  $\text{\AA}^{-1}$  for each atom. For the CsPbBr<sub>3</sub> (110) and TiO<sub>2</sub> (101) slabs, a  $6 \times 3 \times 1$  and  $3 \times 9 \times 1$  k-point mesh was used, respectively. A 30  $\text{\AA}$  vacuum layer along the z direction was adopted to prevent unintended periodic interactions between adjacent slabs. The CsPbBr<sub>3</sub>/TiO<sub>2</sub> heterostructure model

consists two CsPbBr<sub>3</sub> layers and one TiO<sub>2</sub> layer, with a 20  $\text{\AA}$  vacuum space along the z direction. To saving computing resources, a  $1 \times 1 \times 1$  k-point mesh was employed for CsPbBr<sub>3</sub>/TiO<sub>2</sub> heterostructure. The van der Waals interactions between TiO<sub>2</sub> and CsPbBr<sub>3</sub> were taken into account using the DFT-D3 correction method.

### Photocatalytic activity measurements

All photocatalytic reactions were conducted in a quartz reactor. Typically, 10 mg photocatalyst and 1 mL toluene (9.4 mmol) were dispersed in a reactor containing 2 mL acetonitrile. The reactor was purged with O<sub>2</sub> for 10 min, and then irradiated by visible light ( $\lambda > 420$  nm) with a 300 W Xe lamp (CEL-PF300-T8, Beijing China Education Au-light Co., Ltd.). After light irradiation of 2 h, the liquid product was analyzed by a gas chromatography (GC-2030, Shimadzu, Japan, FID detector, nitrogen (N<sub>2</sub>) as carrier gas) after centrifuging the suspension at 10000 rpm for 3 min.

## Results and discussion

### Characterizations of catalysts

The 3D hierarchical CPB/TiO<sub>2</sub> heterostructure was prepared by a simple anti-solvent precipitation method with the addition of TiO<sub>2</sub> nanoflowers into the precursor solution of CsPbBr<sub>3</sub>, as schematically illustrated in **Fig. 1a**. X-ray diffraction (XRD) was exploited to characterize the crystal structure of the blank CsPbBr<sub>3</sub>, CPB/TiO<sub>2</sub> composites and TiO<sub>2</sub>. As shown in **Fig. 1b**, the diffraction peaks at  $15.1^\circ$ ,  $21.5^\circ$ ,  $30.7^\circ$ ,  $34.4^\circ$ , and  $43.8^\circ$  can be ascribed to monoclinic CsPbBr<sub>3</sub> (100), (110), (200), (210) and

(220) planes (JCPDS No. 18-0364).<sup>36-38</sup> In addition, the peaks at  $25.3^\circ$ ,  $37.7^\circ$ ,  $48.0^\circ$ ,  $53.8^\circ$ ,  $55.0^\circ$ ,  $62.6^\circ$  can be attributed to the (101), (004), (200), (105), (211), and (204) planes of anatase TiO<sub>2</sub>, respectively.<sup>32</sup> The XRD patterns of CPB/TiO<sub>2</sub> composites indicate both characteristic peaks of CsPbBr<sub>3</sub> and TiO<sub>2</sub>, and the peaks intensity of the CsPbBr<sub>3</sub> increases as the CsPbBr<sub>3</sub> content increasing (**Fig. S1†**).

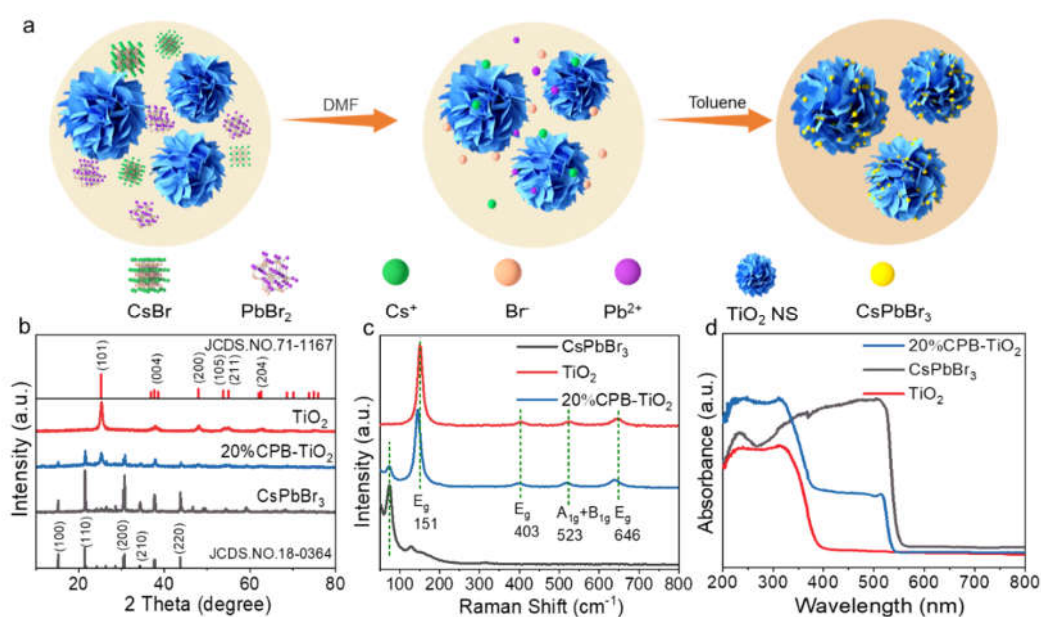


**Fig. 1.** (a) Schematic diagram for the synthesis of 3D nanoflower-shaped CPB/TiO<sub>2</sub> heterostructure. (b) XRD patterns, (c) Raman spectra, and (d) UV-Vis DRS spectra of CsPbBr<sub>3</sub>, CPB/TiO<sub>2</sub> and TiO<sub>2</sub>.

Raman spectra was used to further confirm the composition of the synthesized catalysts. As shown in **Fig. 1c**, the peaks at  $151\text{ cm}^{-1}$  ( $E_g$ ),  $403\text{ cm}^{-1}$  ( $E_g$ ),  $523\text{ cm}^{-1}$  ( $A_{1g}+B_{1g}$ ), and  $646\text{ cm}^{-1}$  ( $E_g$ ) belong to the anatase  $\text{TiO}_2$  vibration modes. A new peak of  $74\text{ cm}^{-1}$  assigned to the vibrational mode of  $[\text{PbBr}_6]^{4-}$  octahedron of  $\text{CsPbBr}_3$  is observed in the  $\text{CPB}/\text{TiO}_2$ .<sup>39-41</sup> The characteristic peak of  $\text{CsPbBr}_3$  is also enhanced with the increment of the loading amount of  $\text{CsPbBr}_3$  (**Fig. S2†**). This coincides with the XRD analysis, validating the successful preparation of the  $\text{CPB}/\text{TiO}_2$  composites. Notably, after the growth of  $\text{CsPbBr}_3$  on the  $\text{TiO}_2$  nanosheets, the Raman peaks of  $\text{TiO}_2$  shift to a lower wavenumber compared to that of blank  $\text{TiO}_2$ . The shift indicates an increasing of bond length and decreasing of the bond energy of the  $\text{Ti}-\text{O}$  bond, which can be attributed to the strong electrostatic interaction between the  $\text{CsPbBr}_3$  and the  $\text{TiO}_2$ .<sup>42-45</sup> **Fig. 1d** shows the UV-vis diffuse reflectance spectroscopy (DRS) analysis of the samples, which is employed to assess the optical absorption properties. It can be seen that the light absorption edge of blank  $\text{TiO}_2$  is around 390 nm, denoting its UV light

response nature. After integrating with  $\text{CsPbBr}_3$ , the light absorption of  $\text{CPB}/\text{TiO}_2$  is extended to approximately 540 nm. Meantime, the absorption edge of  $\text{TiO}_2$  at 390 nm can also be detected. This should be ascribed to the hybridization of high weight content of  $\text{CsPbBr}_3$  with  $\text{TiO}_2$  support. As such, both absorption features are present in the composite. The greatly extended light absorption enables the visible-light-excitation of the  $\text{CPB}/\text{TiO}_2$  composites to be possible, which is beneficial for promoting the solar energy utilization. With the increase of  $\text{CsPbBr}_3$  content, the visible light absorption of  $\text{CPB}/\text{TiO}_2$  is also gradually enhanced (**Fig. S3†**). Moreover, in comparison with blank  $\text{CsPbBr}_3$ , it is notable that the visible light absorption edge of the hybrid  $\text{CPB}/\text{TiO}_2$  composite is slightly blue shifted (*ca.* 14 nm). This can be attributed to the quantum size effect resulted from the smaller size of  $\text{CsPbBr}_3$  in the composite. The inference has been demonstrated by the following scanning electron microscopy (SEM) and transmission electron microscopy (TEM) analyses.

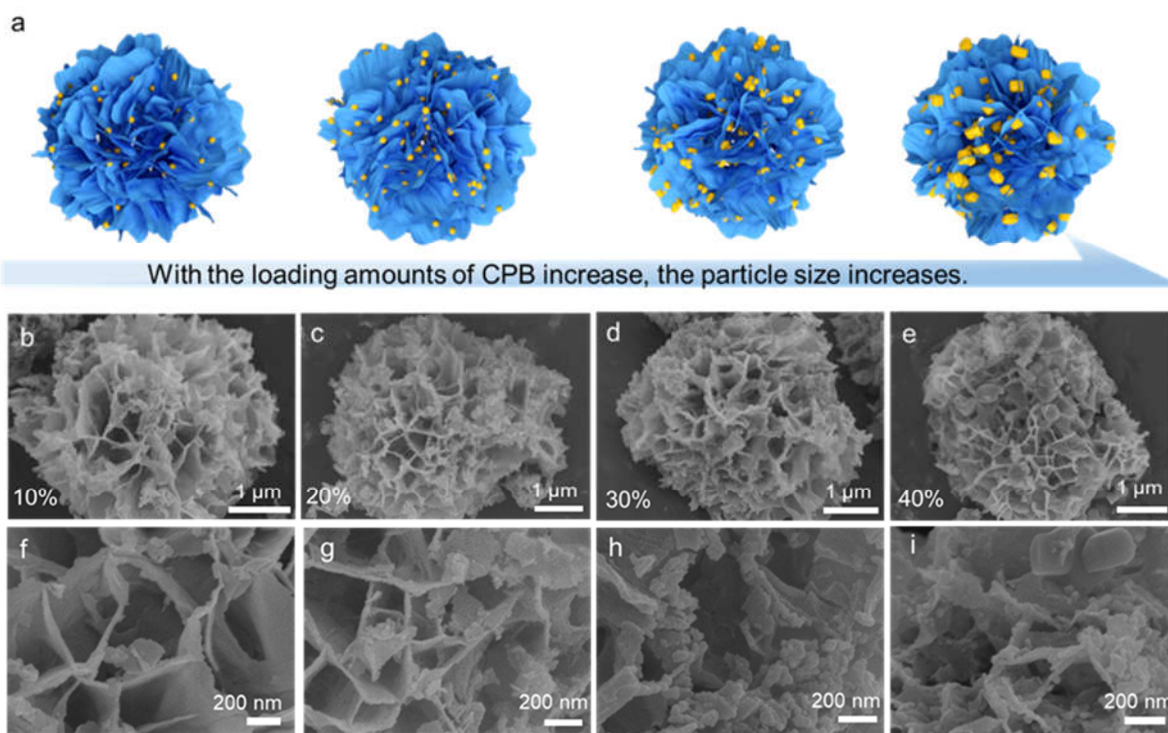


**Fig. 2.** (a) Schematic and (b-i) SEM images showing the morphology evolution of  $x\%$   $\text{CPB}/\text{TiO}_2$  ( $x = 10, 20, 30, 40$ ) composites.

As shown in **Fig. 2** and **Fig. S4-S5†**, SEM is firstly utilized to characterize the morphology and microstructure of the  $\text{CPB}/\text{TiO}_2$ , blank  $\text{TiO}_2$  and  $\text{CsPbBr}_3$  samples. The blank  $\text{TiO}_2$  presents a nanoflower shape, which is assembled by vertical nanoflakes (**Fig. S4†**). The surface of the nanoflakes subunits is clean and smooth. For blank  $\text{CsPbBr}_3$ , it shows a large particle morphology and the particle sizes range from 0.9 to 2.0  $\mu\text{m}$  (**Fig. S5†**). After the construction of the  $\text{CPB}/\text{TiO}_2$  heterojunction, the

$\text{TiO}_2$  nanoflower-shaped structure is maintained (**Fig. 2**), while the surface of the nanoflakes subunits becomes rough due to the in-situ growth of  $\text{CsPbBr}_3$ . From **Fig. 2b-2i**, it can be clearly seen that for all the  $\text{CPB}/\text{TiO}_2$  samples, the sizes of the  $\text{CsPbBr}_3$  particles in the composites are much smaller than that of blank  $\text{CsPbBr}_3$ , indicating that the formation of heterojunction is beneficial for preventing the aggregation and reducing the size of the  $\text{CsPbBr}_3$  halide perovskite. This can be ascribed to that

the presence of TiO<sub>2</sub> nanoflower with nanoflakes subunits can act as heterogeneous nuclei site to facilitate the nucleation and growth of the CsPbBr<sub>3</sub>, which generates more seeds and leads to the smaller size of the CsPbBr<sub>3</sub> particles.<sup>20</sup> The significantly decreased particle size could greatly promote the exposure of surface active sites and inhibit the charge recombination of CsPbBr<sub>3</sub> under light irradiation. Moreover, it is notable that with the increase of the CsPbBr<sub>3</sub> contents from 10% to 40% in the composites, the particle sizes of CsPbBr<sub>3</sub> are increased, as schematically illustrated in Fig. 2a. This can be attributed to the further growth of CsPbBr<sub>3</sub> at high concentrations.

To further obtain the microscopic structure information of the samples, transmission electron microscopy (TEM) analysis is carried out. Taking the 20%CPB/TiO<sub>2</sub> as an example, the TEM image of the sample (Fig. 3a and b) shows a nanoflakes structure of TiO<sub>2</sub>. The surface is rough and densely covered by small CsPbBr<sub>3</sub> nanoparticles. Since that the sample for TEM analysis is prepared by strong ultrasonication, the well-defined CsPbBr<sub>3</sub> nanoparticles on the 2D nanoflakes surface indicates intimate interfacial contact between the two components. Meanwhile, the intensive coverage of CsPbBr<sub>3</sub> forms large contact interface with TiO<sub>2</sub> nanoflakes, which is conducive to

the migration of charge carriers across the CPB/TiO<sub>2</sub> heterojunction.<sup>46</sup> Moreover, nanopores can be observed on the CPB/TiO<sub>2</sub>, which is resulted from the mesoporous structure of the TiO<sub>2</sub> nanoflakes, as demonstrated by the N<sub>2</sub> adsorption-desorption analysis (Fig. S6†). High-resolution TEM (HRTEM) image (Fig. 3c) shows distinct lattice fringe of 0.35 nm and 0.41 nm, corresponding to the (101) planes and (110) planes of anatase TiO<sub>2</sub> and monoclinic CsPbBr<sub>3</sub>, respectively. Furthermore, Fig. 3d shows the corresponding energy dispersive X-ray spectroscopy (EDS) elemental mappings analysis of the 20%CPB/TiO<sub>2</sub>. Cs, Pb, Br, Ti and O elements are uniformly distributed on the nanoflakes structure, indicating that CsPbBr<sub>3</sub> and TiO<sub>2</sub> are well combined. The results further verify the formation of CPB/TiO<sub>2</sub> hybrid composite with intimate interfacial contact. Moreover, in comparison with blank TiO<sub>2</sub>, the 20%CPB/TiO<sub>2</sub> composite displays smaller specific surface area (Table S1†), which can be attributed to that the growth of CsPbBr<sub>3</sub> nanoparticles on the surface of TiO<sub>2</sub> may aggregate in the TiO<sub>2</sub> pores. Correspondingly, the total pore volume of 20%CPB/TiO<sub>2</sub> is also slightly lower than that of blank TiO<sub>2</sub>. The result matches with the SEM measurement.

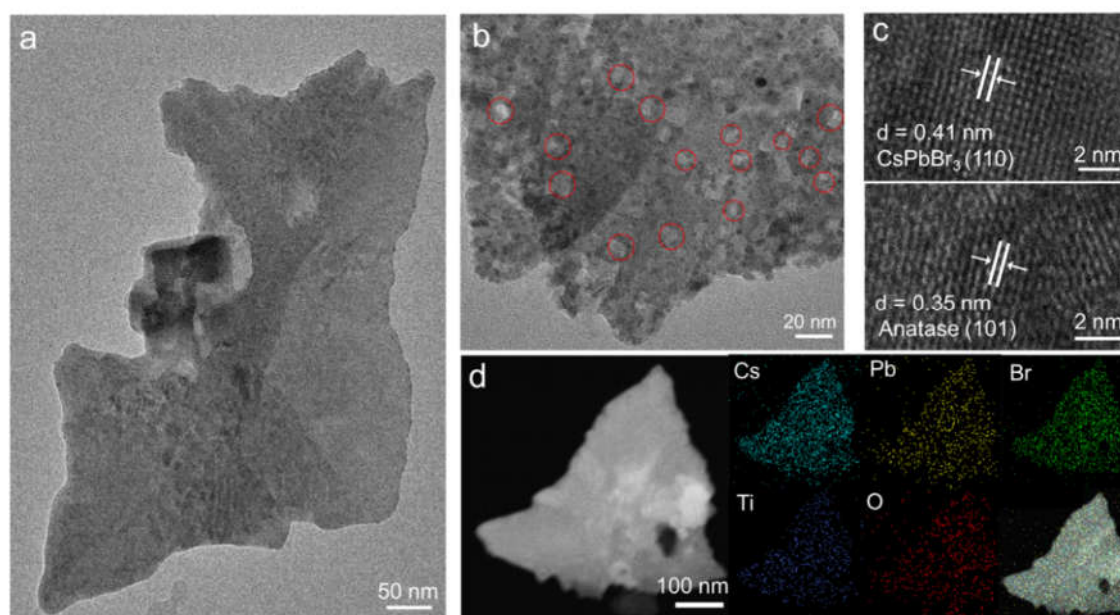


Fig. 3. (a, b) TEM images, (c) HRTEM image, and (d) corresponding EDS elemental mapping images of 20%CPB/TiO<sub>2</sub>.

To study the surface chemical states of the samples, X-ray photoelectron spectroscopy (XPS) has been performed. As shown in Fig. 4a, the presence of Cs, Pb, Br, O and Ti elements can be detected from the XPS survey spectrum of CPB/TiO<sub>2</sub>. The high-resolution spectrum of Ti 2p shows two peaks of Ti 2p<sub>3/2</sub> and Ti 2p<sub>1/2</sub> at 458.5 eV and 464.2 eV (Fig. 4b), which indicates that Ti element mainly exists as Ti<sup>4+</sup> ions. For the O 1s pattern (Fig. 4c), it can be divided into two peaks, which are attributed to the lattice O (Ti–O) and hydroxyl O (–OH). Fig. S7† shows the fine-scanned Cs 3d XPS spectrum, the two peaks with binding energies at 724.2 eV and 738.1 eV are assigned to Cs 3d<sub>5/2</sub> and

Cs 3d<sub>3/2</sub>, indicating that the chemical state of the Cs in the composite is +1. The Pb 4f spectrum in Fig. 4d shows characteristic peaks at 138.0 eV and 142.9 eV, corresponding to Pb 4f<sub>7/2</sub> and Pb 4f<sub>5/2</sub> orbitals of Pb<sup>2+</sup> ion. Moreover, the Br 3d is decomposed into two peaks at 67.9 eV and 68.9 eV, corresponding to the binding energies of Br 3d<sub>5/2</sub> and 3d<sub>3/2</sub>, attributed to the presence of Br<sup>–</sup> (Fig. 4e). It is worth noting that for the CPB/TiO<sub>2</sub> composite, the Ti 2p and O 1s peaks show a negative shift of 0.2 eV in comparison with blank TiO<sub>2</sub> (Fig. 4b and c). In contrast, the binding energies of Cs 4d, Pb 4f, and Br 3d in the CPB/TiO<sub>2</sub> show a positive shift (Fig. 4d–e and S7†),

which are higher than those of blank CsPbBr<sub>3</sub> by 0.4 eV. The results verify the strongly interacted interface with electron transfer from the CsPbBr<sub>3</sub> to the TiO<sub>2</sub> nanosheets in the heterostructure, which is in accordance with the Raman analysis. To further clarify the interaction and electron transfer at the interface, density functional theory (DFT) calculation has been carried out. Fig. 4g and h shows the work functions of the TiO<sub>2</sub> (101) and CsPbBr<sub>3</sub> (110) slabs, which are 7.09 eV and 4.63 eV, respectively, corresponding to the Fermi levels ( $E_f$ ) of -3.61 eV and -2.51 eV (vs. the vacuum level). Due to the lower  $E_f$  value

of TiO<sub>2</sub> than that of blank CsPbBr<sub>3</sub>, the electrons would be migrated from the CsPbBr<sub>3</sub> to the TiO<sub>2</sub> at the heterojunction interface until their  $E_f$  are aligned. Similar result is obtained from the calculated planar-averaged charge density difference of CPB/TiO<sub>2</sub>. As shown in Fig. 4f, the light cyan and yellow regions indicate the charge depletion and accumulation area, respectively. The calculation results reveal that the cyan region is mainly on the CsPbBr<sub>3</sub> side, while the yellow region is on the TiO<sub>2</sub> side, further validating the transfer of electrons from CsPbBr<sub>3</sub> to TiO<sub>2</sub>. This is consistent with the XPS analysis results.

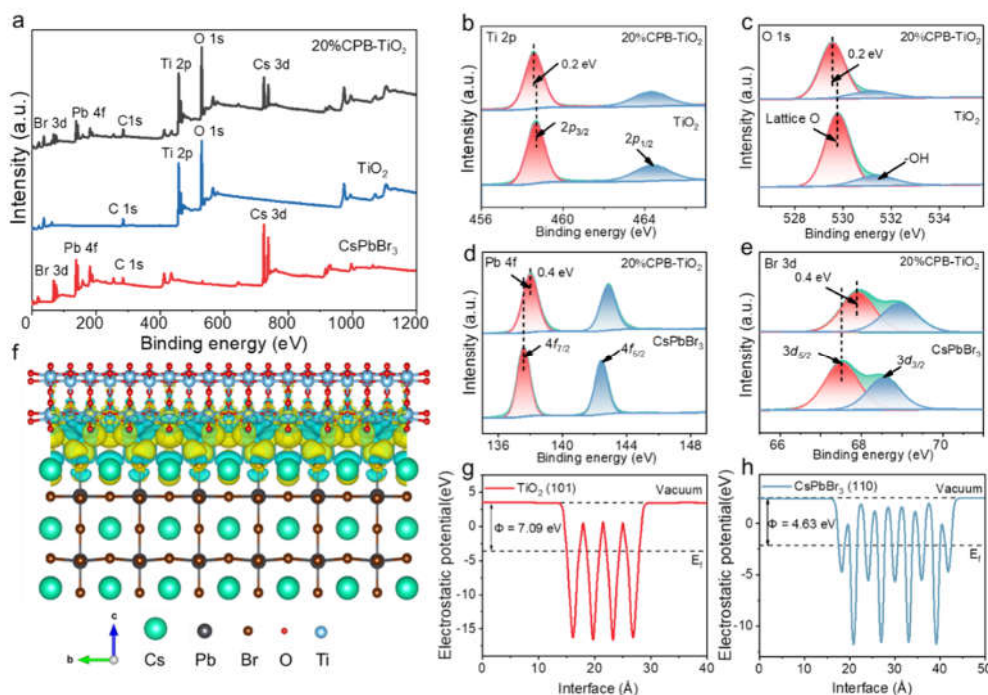


**Fig. 4.** XPS spectra of CsPbBr<sub>3</sub>, TiO<sub>2</sub> and 20%CPB/TiO<sub>2</sub>: (a) survey, (b) Ti 2p, (c) O 1s, (d) Pb 4f and (e) Br 3d. (f) Charge density differences in the CPB/TiO<sub>2</sub> composite. (g, h) The work functions of blank TiO<sub>2</sub> and CsPbBr<sub>3</sub>.

### Photocatalytic performances

Collectively, the above characterizations faithfully verify the successful fabrication of CPB/TiO<sub>2</sub> hybrid composites with intimate interfacial contact and strong chemical interaction. The presence of TiO<sub>2</sub> nanoflower with 2D nanoflakes subunits greatly inhibits the agglomeration of the halide perovskites, while the CsPbBr<sub>3</sub> extends the light absorption range of TiO<sub>2</sub>. In view of the desired structural and optical properties, the photocatalytic oxidation of toluene over the hybrid CPB/TiO<sub>2</sub> composites has been tested. A 300 W Xeon lamp equipped with a 420 nm cutoff filter is utilized as a visible light source. It is well known that the solvent/reactant ratio has great influence on the oxidation of toluene,<sup>2,47</sup> thus, the reaction condition of different acetonitrile/toluene ratio is firstly optimized using the 20%CPB/TiO<sub>2</sub> as an example. As shown in Fig. 5a, as the ratio of toluene increases from 0.3 to 1 mL, the photoactivity of the 20%CPB/TiO<sub>2</sub> composite gradually increases. The catalyst shows the highest toluene conversion rate of 10200  $\mu\text{mol g}^{-1} \text{h}^{-1}$  when

the volume ratio of acetonitrile solvent and toluene reactant is 2:1. The enhanced photoactivity can be attributed to that the increased toluene concentration enhances the reaction possibility between the photogenerated charge carriers and the toluene molecules. However, further increase of the toluene to 1.5 mL and 2 mL decreases the conversion rate. This might be ascribed to the excess adsorption of toluene reactant on the catalyst surface, which would slow down the desorption of the BA and BAD products and suppress the oxidation activity.<sup>48</sup> Based on the result, the following photoactivity tests of all the other samples are carried out under the optimized condition with the acetonitrile/toluene ratio of 2:1.

Fig. 5b shows the visible-light-driven photocatalytic performances of the blank CsPbBr<sub>3</sub> and the CPB/TiO<sub>2</sub> composites with different ratios of CPB for the selective oxidation of toluene. The blank CsPbBr<sub>3</sub> exhibits a low activity with generation rates of 390  $\mu\text{mol g}^{-1} \text{h}^{-1}$  for BAD and 130  $\mu\text{mol g}^{-1} \text{h}^{-1}$  for BA. The unsatisfactory photocatalytic performance should be due to the severe charge recombination caused by

the large particle size of CsPbBr<sub>3</sub>. For blank TiO<sub>2</sub>, it presents no activity. This is reasonable since that the TiO<sub>2</sub> has no visible light absorption and cannot be excited by visible light. In contrast, after the hybridization of CsPbBr<sub>3</sub> with TiO<sub>2</sub>, the photocatalytic performances of all the hierarchical CPB/TiO<sub>2</sub> heterojunctions are significantly improved. The best photocatalytic toluene oxidation activity is achieved over the 20%CPB/TiO<sub>2</sub> composite, which shows a toluene conversion rate of 10200 μmol g<sup>-1</sup> h<sup>-1</sup> (BAD production rate of 8670 μmol g<sup>-1</sup> h<sup>-1</sup> and BA generation rate of 1530 μmol g<sup>-1</sup> h<sup>-1</sup>). The photoactivity is about 20 times higher than blank CsPbBr<sub>3</sub>, which is also among the top photocatalytic performance reported so far for UV and visible-light-driven selective oxidation of toluene (Fig. 5c and Table S2 †). The apparent quantum efficiency (AQE) of the 20%CsPbBr<sub>3</sub>/TiO<sub>2</sub> composite reaches 2.9% at λ = 420 nm for the

transformation of toluene into BA and BAD (Fig. S14 †). The gas chromatography-mass (GC-MS) analysis of the reaction solution after light irradiation reveals four peaks, which are ascribed to acetonitrile solvent, toluene reactant, BAD and BA products (Fig. S8 †). No other product or intermediate is detected, validating the high selectivity of the reaction. With the increase of CsPbBr<sub>3</sub> loading to higher contents (30% and 40%), it results in a performance degradation. This may be ascribed to that: (1) an excess of halide perovskite tends to aggregate into large particles, which will lead to longer migration distances of charge carriers and increase charge recombination; (2) the coverage of excessive and oversized CsPbBr<sub>3</sub> on TiO<sub>2</sub> surface will lead to the reduction of the exposed surface area, inhibiting the adsorption of toluene molecules.

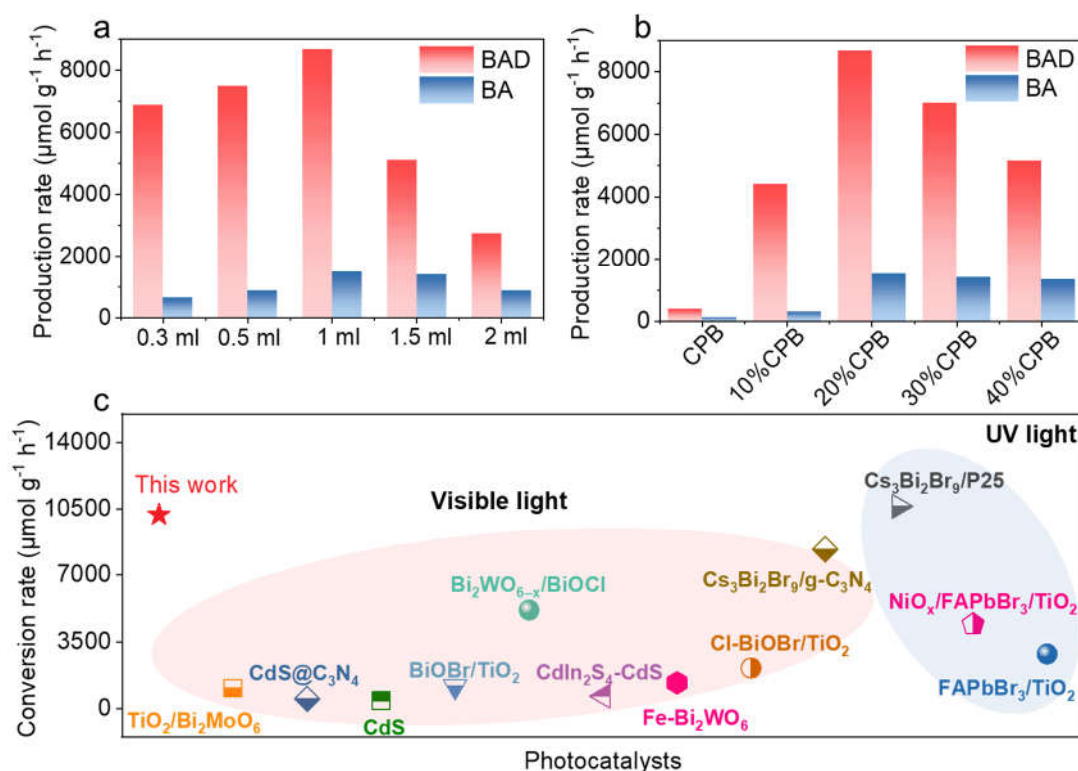


Fig. 5. (a) Photocatalytic oxidation of toluene with different toluene amount in acetonitrile solvent over 20%CPB/TiO<sub>2</sub>. The total volume is 3 ml. (b) Photocatalytic oxidation of toluene over blank TiO<sub>2</sub>, CPB/TiO<sub>2</sub> composite and blank CsPbBr<sub>3</sub>. (c) Performance comparison with reported photocatalysts for UV and visible-light-driven selective oxidation of toluene.

Furthermore, the broad applicability of the CPB/TiO<sub>2</sub> photocatalyst is investigated for photocatalytic selective oxidation of C(sp<sup>3</sup>)-H of toluene derivatives with different substituents. As shown in Table 1, these aromatics are efficiently converted into corresponding aldehydes and alcohols. The selectivity for the aldehyde product is higher than 70%. Notably, the substrate with electron-withdrawing substituents (-F, -Cl, -Br) displays lower photocatalytic activity. This can be attributed to that the electron-withdrawing groups on benzene ring inhibit the abstraction of hydrogen from the methyl group.<sup>49-50</sup> In addition, p-xylene shows a higher toluene conversion rate (12746 μmol g<sup>-1</sup> h<sup>-1</sup>) than its isomers of o-xylene (9900 μmol

g<sup>-1</sup> h<sup>-1</sup>) and m-xylene (10930 μmol g<sup>-1</sup> h<sup>-1</sup>), which can be attributed to the steric hindrance of the methyl groups hindering the reactant adsorption and activation on the catalyst surface.<sup>51,52</sup>

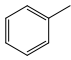
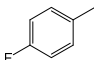
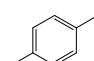
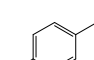
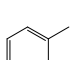
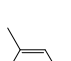
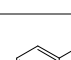
Moreover, the cycle test of the 20%CsPbBr<sub>3</sub>/TiO<sub>2</sub> has been carried out. After repeating the photoactivity test for 4 cycles (Fig. S16 †), the catalyst still maintains a high activity with negligible decrease in the conversion rate of toluene. In addition, the used 20%CsPbBr<sub>3</sub>/TiO<sub>2</sub> has been further characterized by XRD and XPS (Fig. S17 †–S18 †). No obvious change in the crystal structure and surface chemical state is

observed for the composite before and after reaction. These results validate the high stability of the CsPbBr<sub>3</sub>/TiO<sub>2</sub> composite.

### Photoelectric properties

In order to better understand the reasons for the improved photocatalytic performance, the band structures of the CsPbBr<sub>3</sub> and the TiO<sub>2</sub> are investigated by Mott-Schottky (M-S) measurement and DRS analysis. As shown in Fig. 6a and b, the positive slopes indicate that CsPbBr<sub>3</sub> and TiO<sub>2</sub> are typical n-type semiconductors.<sup>53</sup> The flat band potential ( $E_{FB}$ ) are calculated to be -0.86 V and -0.34 V (vs. NHE) for CsPbBr<sub>3</sub> and TiO<sub>2</sub>, respectively. Usually, the conduction band potential ( $E_{CB}$ ) for n-type semiconductor is more negative of about 0.1 eV than  $E_{FB}$ .<sup>54</sup> Thus, the  $E_{CB}$  of CsPbBr<sub>3</sub> and TiO<sub>2</sub> are concluded to -0.96 V and -0.44 V (vs. NHE), respectively. In addition, the corresponding bandgaps of TiO<sub>2</sub> and CsPbBr<sub>3</sub> are estimated by Tauc plots transformed from the DRS spectra (Fig. S9†), which are 3.20 eV and 2.28 eV, respectively. Based on these, the valance band positions ( $E_{VB}$ ) of CsPbBr<sub>3</sub> and TiO<sub>2</sub> can be calculated as 1.32 V and 2.76 V. As a result, a type-II heterojunction is formed between the CsPbBr<sub>3</sub> and the TiO<sub>2</sub> because of the staggered band structures.

Table 1. Photocatalytic oxidation of C(sp<sup>3</sup>)-H in substituted toluene over 20%CPB/TiO<sub>2</sub>.<sup>a</sup>

Entry	Substrates	Conversion rate ( $\mu\text{mol g}^{-1} \text{h}^{-1}$ )	Selectivity (%)	
			A	B
1		10200	85	15
2		5950	83	17
3		9040	88	12
4		9770	87	13
5		9900	76	24
6		10930	72	28
7		12746	71	29

<sup>a</sup> Reaction conditions: catalyst (10 mg 20%CPB/TiO<sub>2</sub>), substrate (1 mL), MeCN (2 mL), 1 atm of O<sub>2</sub>, 2 h irradiation with visible light ( $\lambda > 420 \text{ nm}$ ).

To study the influence of the heterojunction structure on the transfer behavior of photogenerated charge carriers, transient photocurrent and electrochemical impedance spectra (EIS) tests are performed. As shown in Fig. 6c, under visible light irradiation, both CsPbBr<sub>3</sub> and CPB/TiO<sub>2</sub> show rapid and stable photocurrent responses, while TiO<sub>2</sub> does not. This can be attributed to the inability of TiO<sub>2</sub> to be excited by visible light (Fig. 1d). In addition, the photocurrent intensity of blank CsPbBr<sub>3</sub> is markedly lower than that of 20% CPB/TiO<sub>2</sub>. This should be due to the agglomerated large particle size of the blank CsPbBr<sub>3</sub>, which leads to a severe recombination of photogenerated charge carriers.<sup>54</sup> Moreover, Fig. 6d shows the Nyquist plots of the samples, which is employed to investigate the interfacial charge transfer efficiency.<sup>55</sup> In general, the smaller diameter of the semicircular arc in the Nyquist plots reflects the lower electron transfer resistance. It can be found that the 20%CPB/TiO<sub>2</sub> sample has the minimum arc radius, which means the best electronic conductivity and charge separation ability.<sup>56,57</sup> Furthermore, the steady-state photoluminescence (PL) spectra are also used to examine the charge separation efficiency. As shown in Fig. S19†, the 20%CsPbBr<sub>3</sub>/TiO<sub>2</sub> composite shows a much lower PL intensity than CsPbBr<sub>3</sub>, revealing that the charge recombination is significantly suppressed in the composite. In addition, the TiO<sub>2</sub> shows no obvious PL signal. This is in accordance with the photocurrent analysis that the TiO<sub>2</sub> is unable to be excited to generate charge carriers by visible light. These photoelectrochemical findings highlight that the construction of the type-II heterojunction between CsPbBr<sub>3</sub> and TiO<sub>2</sub> could effectively accelerate charge transfer, thus contributing to improving the photocatalytic performance.

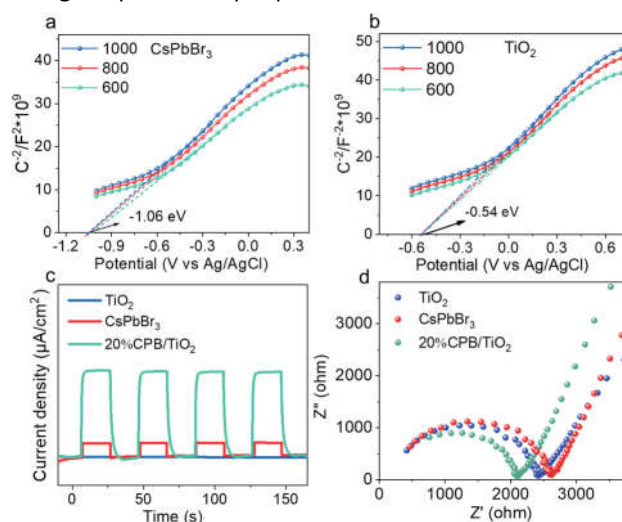
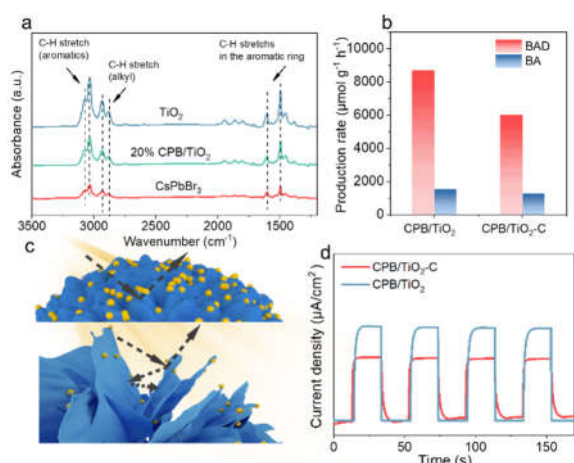


Fig. 6. (a, b) M-S plots of CsPbBr<sub>3</sub> and TiO<sub>2</sub>. (c) Transient photocurrent responses, and (d) EIS Nyquist plots of blank TiO<sub>2</sub>, CsPbBr<sub>3</sub> and CPB/TiO<sub>2</sub> composite.

Furthermore, for heterogeneous photocatalytic reactions, the effective adsorption of reactant on the catalyst surface is another requisite for the ignition of the redox reaction.<sup>23, 58-60</sup> The BET surface area and porous structure analyses of the TiO<sub>2</sub>, CsPbBr<sub>3</sub> and 20%CPB/TiO<sub>2</sub> samples have shown that the



introduction of  $\text{TiO}_2$  nanoflower significantly improves the specific surface area and pore volume of 20%CPB/ $\text{TiO}_2$  in comparison with that of blank  $\text{TiO}_2$  (Fig. S6† and Table S1†). Generally, larger specific surface area and porous structure enables better adsorption capacity, and exposure of more active sites of catalysts. To further reveal the contribution of the heterostructure for the reactant adsorption, Fourier transform infrared (FTIR) spectroscopy is used to identify the adsorbed toluene species on the  $\text{CsPbBr}_3$ ,  $\text{TiO}_2$  and 20%CPB/ $\text{TiO}_2$  surface. As shown in Fig. 7a, for all the three samples after adsorption equilibrium, the typical absorption peaks of toluene are observed, including the C–H stretching vibration of the aromatic ring at 3083 and 3038  $\text{cm}^{-1}$ , the skeleton vibration of aromatic ring at 1606 and 1495  $\text{cm}^{-1}$ , and the C–H symmetric and asymmetric stretching of methylene group at 2934 and 2875  $\text{cm}^{-1}$ .<sup>61–62</sup> Notably, the signal of toluene molecules of 20%CPB/ $\text{TiO}_2$  is obviously higher than that of blank  $\text{CsPbBr}_3$ , yet is lower than blank  $\text{TiO}_2$ . The result indicates that the introduction of  $\text{TiO}_2$  can promote the toluene adsorption capacity of CPB/ $\text{TiO}_2$ , which is conducive to the catalytic conversion.



**Fig. 7.** (a) FTIR spectra of 20%CPB/ $\text{TiO}_2$ ,  $\text{TiO}_2$  and  $\text{CsPbBr}_3$  after adsorption of saturated toluene. (b) Photoactivity comparison between CPB/ $\text{TiO}_2$  and CPB/ $\text{TiO}_2$ -C. (c) Schematic diagram of light absorption over CPB/ $\text{TiO}_2$  and CPB/ $\text{TiO}_2$ -C. (d) Transient photocurrent responses of CPB/ $\text{TiO}_2$  and CPB/ $\text{TiO}_2$ -C.

Finally, to investigate the influence of the hierarchical flower-like nanostructure constructed by 2D nanoflakes subunits on the photocatalytic performance, a collapsed 20%CPB/ $\text{TiO}_2$  catalyst (marked as 20%CPB/ $\text{TiO}_2$ -C) without such structure has been fabricated for comparison. As shown in Fig. 7b, the photoactivity test reveals that the 20%CPB/ $\text{TiO}_2$ -C has a BAD generation rate of  $6000 \mu\text{mol g}^{-1} \text{h}^{-1}$  and a BA production rate of  $1250 \mu\text{mol g}^{-1} \text{h}^{-1}$ , which is notably lower than the CPB/ $\text{TiO}_2$ . Fig. S10† shows the morphology analysis of the 20%CPB/ $\text{TiO}_2$ -C, which reveals a bulky grain structure with a rough surface.  $\text{CsPbBr}_3$  nanoparticles are dispersed on the surface of the massive  $\text{TiO}_2$ . The size of the  $\text{CsPbBr}_3$  particles in the composite is also much smaller than that of blank  $\text{CsPbBr}_3$ , which once again proves that  $\text{TiO}_2$  plays a critical role in inhibiting the growth of  $\text{CsPbBr}_3$ . Nevertheless, compared with 20%CPB/ $\text{TiO}_2$ ,

the size of the  $\text{CsPbBr}_3$  particles is much larger in the 20%CPB/ $\text{TiO}_2$ -C. The result validates that the  $\text{TiO}_2$  nanoflakes are more beneficial in preventing the agglomeration of the  $\text{CsPbBr}_3$  particles.

In addition, UV-vis DRS is performed to study the optical absorption property of the 20%CPB/ $\text{TiO}_2$ -C. The sample shows a similar absorption edge as that of 20%CPB/ $\text{TiO}_2$ , but the light absorption intensity in the range of 200–550 nm is lower (Fig. S11†). The result indicates that the 3D hierarchical CPB/ $\text{TiO}_2$  structure is more efficient for solar energy collection, which can be attributed to the multiple light reflection and refraction caused by the vertical nanoflakes, as schematically illustrated in Fig. 7c. Meanwhile, the transient photocurrent response test displays that the 20%CPB/ $\text{TiO}_2$  exhibits a higher photocurrent density than that of CPB/ $\text{TiO}_2$ -C under visible light irradiation, indicating more efficient charge transfer (Fig. 7d). This can be related to the fact that  $\text{TiO}_2$  nanoflakes facilitates the formation of smaller  $\text{CsPbBr}_3$  particle, which could shorten the charge transfer distance to the surface and promote the interfacial charge separation. Hence, to sum up, the construction of the unique hierarchical CPB/ $\text{TiO}_2$  structure greatly enhances the photocatalytic performance due to the existence of  $\text{TiO}_2$  nanoflakes, which (1) greatly prohibits the aggregation of the  $\text{CsPbBr}_3$ , forming much smaller perovskite particles that shorten the charge transfer distance; (2) heightens light absorption by the multiple reflection and scattering between the nanoflakes structure that benefits the solar energy harvesting and conversion; (3) enhances the adsorption of toluene molecules and promotes the surface reaction rates.

### Photocatalytic Mechanism

To elucidate the photocatalytic mechanism of toluene oxidation over the CPB/ $\text{TiO}_2$  photocatalyst, a series of control experiments have been conducted in the absence of  $\text{O}_2$  or with the addition of specific radical scavengers. As shown in Fig. 8a, the toluene oxidation is almost completely suppressed when  $\text{O}_2$  is replaced by Ar, indicating that  $\text{O}_2$  is indispensable. When isopropanol (IPA) is added into the reaction system as a scavenger of hydroxyl radicals ( $\bullet\text{OH}$ ), it has almost no effect on toluene conversion, suggesting that  $\bullet\text{OH}$  is rarely involved in the reaction. In contrast, whether adding ammonium oxalate (AO) to eliminate holes ( $\text{h}^+$ ) or butylated hydroxytoluene (BHT) to capture carbon-centered radicals, the reaction rate significantly reduces. Besides, the toluene conversion is also significantly decreased when BQ is added as superoxide free radical ( $\bullet\text{O}_2^-$ ) scavenger. The above results clearly indicate that  $\bullet\text{O}_2^-$ ,  $\text{h}^+$ , and carbon-centered radicals play key roles in the photocatalytic selective oxidation of toluene.

Subsequently, to further identify the existence of  $\bullet\text{O}_2^-$ , electron paramagnetic resonance (EPR) spectroscopy was employed using 5,5-dimethyl-pyrroline-N-oxide (DMPO) as a trapping agent. As shown in Fig. S12† and Fig. 8b, no DMPO- $\bullet\text{O}_2^-$  signal is detected in dark condition. After visible light irradiation, distinct signals of DMPO- $\bullet\text{O}_2^-$  are observed for both  $\text{CsPbBr}_3$  and CPB/ $\text{TiO}_2$ , while no signals are detected from  $\text{TiO}_2$ . The CPB/ $\text{TiO}_2$  catalyst exhibits a higher ability to generate more  $\bullet\text{O}_2^-$  radicals than pure  $\text{CsPbBr}_3$ , which is important to promote

the oxidation of toluene. Moreover, no DMPO-•OH signal is observed under the same conditions, demonstrating that •OH is absent in the reaction process (Fig. S13† and S15†).

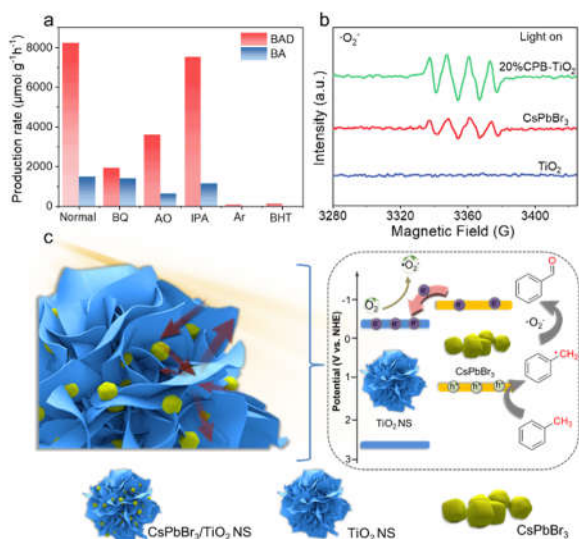


**Fig. 8.** (a) Photocatalytic toluene oxidation in the absence or presence of various radical scavengers. (b) EPR spectra of DMPO- $\text{O}_2^{\bullet-}$ . (c) Schematic illustration of the proposed mechanism of photocatalytic oxidation of toluene over the CPB/TiO<sub>2</sub> composite.

Based on the above analyses, a possible photocatalytic reaction mechanism over the hierarchical CPB/TiO<sub>2</sub> heterojunction is proposed. As schematically illustrated in Fig. 8c, Upon the photoexcitation, electrons and holes are generated in the conduction band (CB) and the valence band (VB) of CsPbBr<sub>3</sub>. Due to the staggered energy bands, the photogenerated electrons in the CB of CsPbBr<sub>3</sub> can efficiently migrate to the CB of TiO<sub>2</sub> and left holes on the VB of CsPbBr<sub>3</sub>, which prolongs the lifetime of the photogenerated charge carriers. After that, molecular O<sub>2</sub> can be activated by electron on the CB of TiO<sub>2</sub>. Meanwhile, photogenerated holes oxidize the toluene to produce benzyl radicals ( $\cdot\text{CH}_2\text{-R}$ ) on the VB of CsPbBr<sub>3</sub>. Then, the  $\text{O}_2^{\bullet-}$  radical reacts with the benzyl radicals to produce benzaldehyde.

## Conclusions

In summary, we have designed and synthesized a hierarchical CPB/TiO<sub>2</sub> heterojunction as advanced photocatalyst for efficient visible-light-driven toluene oxidation by assembling CsPbBr<sub>3</sub> nanoparticles onto nanoflower-shaped TiO<sub>2</sub> with 2D nanoflakes subunits. The formed CPB/TiO<sub>2</sub> composite integrates the structural and electronical merits of the nanoflower-shaped TiO<sub>2</sub> and halide perovskite CsPbBr<sub>3</sub>, which not only enhances the solar light utilization, but also enhances the adsorption of toluene reactant, and boosts the separation and transportation of photogenerated carriers. A high toluene oxidation rate of  $10200 \mu\text{mol g}^{-1} \text{h}^{-1}$  is achieved over the optimal CPB/TiO<sub>2</sub> composite, which is about 20-fold higher than that of blank CsPbBr<sub>3</sub>. The study demonstrates the significance of rational

design of well-defined hierarchical heterojunction catalysts over metal halide perovskites for efficient photocatalytic redox reaction.

## Conflicts of interest

There are no conflicts to declare.

## Acknowledgements

This work was financially supported by the National Key Research and Development Program of China (2019YFC1908203), the National Natural Science Foundation of China (22178057 and 21905049), the Natural Science Foundation of Fujian Province (2020J01201 and 2021J01197), the Research Foundation of the Academy of Carbon Neutrality of Fujian Normal University (TZH2022-07), and the Award Program for Minjiang Scholar Professorship.

## Notes and references

- W. Wu, G. Zhang, J. Zhang, G. Wang, C.-H. Tung and Y. Wang, *Chem. Eng. J.*, 2021, **404**, 126433.
- X. Li, T. Wang, X. Tao, G. Qiu, C. Li and B. Li, *J. Mater. Chem. A*, 2020, **8**, 17657-17669.
- S. Okunaka, H. Tokudome and Y. Hitomi, *J. Catal.*, 2020, **391**, 480-484.
- S. Zhang, W. Huang, X. Fu, X. Zheng, S. Meng, X. Ye and S. Chen, *Appl. Catal., B*, 2018, **233**, 1-10.
- J. Li, B. Ren, X. Yan, P. Li, S. Gao and R. Cao, *J. Catal.*, 2021, **395**, 227-235.
- C. Xu, F. Yang, B. Deng, Y. Zhuang, D. Li, B. Liu, W. Yang and Y. Li, *J. Catal.*, 2020, **383**, 1-12.
- J. Li, S. Zhang, S. Gui, G. Chen, Y. Wang, Z. Wang, X. Zheng, S. Meng, C. Ruan and S. Chen, *Appl. Surf. Sci.*, 2023, **611**, 155616.
- Q. Zhang, J. Wang, X. Ye, Z. Hui, L. Ye, X. Wang and S. Chen, *ACS Appl. Mater. Interfaces*, 2019, **11**, 46735-46745.
- Y. Liu, L. Chen, Q. Yuan, J. He, C. T. Au and S. F. Yin, *Chem. Commun.*, 2016, **52**, 1274-1277.
- M. Zhou, S. Li, S. Wang, Z. Jiang, C. Yang, F. Guo, X. Wang and W.-k. Ho, *Appl. Surf. Sci.*, 2022, **599**, 153985.
- M. Zhang, W. Sun, H. Lv and Z.-H. Zhang, *Curr. Opin. Green Sustain. Chem.*, 2021, **27**, 100390.
- Z. Zhang, Y. Liang, H. Huang, X. Liu, Q. Li, L. Chen and D. Xu, *Angew. Chem. Int. Ed. Engl.*, 2019, **58**, 7263-7267.
- M. Zhang, Z. Li, X. Xin, J. Zhang, Y. Feng and H. Lv, *ACS Catal.*, 2020, **10**, 14793-14800.
- T. Chen, B. Weng, S. Lu, H. Zhu, Z. Chen, L. Shen, M. B. J. Roeffaers and M. Q. Yang, *J. Phys. Chem. Lett.*, 2022, **13**, 6559-6565.
- R. Cheng, J. A. Steele, M. B. J. Roeffaers, J. Hofkens and E. Debroye, *ACS Appl. Energy Mater.*, 2021, **4**, 3460-3468.
- H. Huang, J. Zhao, Y. Du, C. Zhou, M. Zhang, Z. Wang, Y. Weng, J. Long, J. Hofkens, J. A. Steele and M. B. J. Roeffaers, *ACS Nano*, 2020, **14**, 16689-16697.
- H. Huang, H. Yuan, J. Zhao, G. Solís-Fernández, C. Zhou, J. W. Seo, J. Hendrix, E. Debroye, J. A. Steele, J. Hofkens, J. Long and M. B. J. Roeffaers, *ACS Energy Lett.*, 2018, **4**, 203-208.

- 18 H. Huang, H. Yuan, K. P. F. Janssen, G. Solís-Fernández, Y. Wang, C. Y. X. Tan, D. Jonckheere, E. Debroye, J. Long, J. Hendrix, J. Hofkens, J. A. Steele and M. B. J. Roeffaers, *ACS Energy Lett.*, 2018, **3**, 755-759.
- 19 C. Chen, J. Zhou, J. Geng, R. Bao, Z. Wang, J. Xia and H. Li, *Appl. Surf. Sci.*, 2020, **503**, 144287.
- 20 Y. Dai, C. Poidevin, C. Ochoa-Hernandez, A. A. Auer and H. Tuysuz, *Angew. Chem. Int. Ed.*, 2020, **59**, 5788-5796.
- 21 F. Xu, K. Meng, B. Cheng, S. Wang, J. Xu and J. Yu, *Nat. Commun.*, 2020, **11**, 4613.
- 22 M.-Q. Yang, J. Dan, S. J. Pennycook, X. Lu, H. Zhu, Q.-H. Xu, H. J. Fan and G. W. Ho, *Mater. Horiz.*, 2017, **4**, 885-894.
- 23 X. Lin, Z. Xie, B. Su, M. Zheng, W. Dai, Y. Hou, Z. Ding, W. Lin, Y. Fang and S. Wang, *Nanoscale*, 2021, **13**, 18070-18076.
- 24 S. Wang, B. Y. Guan and X. W. Lou, *Energy Environ. Sci.*, 2018, **11**, 306-310.
- 25 L. Zhu, M. Hong and G. W. Ho, *Nano Energy*, 2015, **11**, 28-37.
- 26 L. He, W. Zhang, K. Zhao, S. Liu and Y. Zhao, *J. Mater. Chem. A*, 2022, **10**, 4758-4769.
- 27 Q. Shen, S. Zhou, F.-L. Yang, X. Wang and X. Han, *J. Mater. Chem. A*, 2022, **10**, 4974-4980.
- 28 S. Wang, B. Y. Guan, X. Wang and X. W. D. Lou, *J. Am. Chem. Soc.*, 2018, **140**, 15145-15148.
- 29 S. Wang, B. Y. Guan and X. W. D. Lou, *J. Am. Chem. Soc.*, 2018, **140**, 5037-5040.
- 30 T. Zhu, L. Zhu, J. Wang and G. W. Ho, *J. Mater. Chem. A*, 2016, **4**, 13916-13922.
- 31 Z. Chen, F. Guo, H. Sun, Y. Shi and W. Shi, *J. Colloid Interface Sci.*, 2022, **607**, 1391-1401.
- 32 K. Lan, Y. Liu, W. Zhang, Y. Liu, A. Elzatahry, R. Wang, Y. Xia, D. Al-Dhayan, N. Zheng and D. Zhao, *J. Am. Chem. Soc.*, 2018, **140**, 4135-4143.
- 33 Q. Sun, W. Ye, J. Wei, L. Li, J. Wang, J.-H. He and J.-M. Lu, *J. Alloys Compd.*, 2022, **893**, 162326.
- 34 J. Hafner, *J. Comput. Chem.*, 2008, **29**, 2044-2078.
- 35 G. Kresse and J. Hafner, *Phys. Rev. B Condens. Matter*, 1993, **48**, 13115-13118.
- 36 L. Rao, Y. Tang, C. Yan, J. Li, G. Zhong, K. Tang, B. Yu, Z. Li and J. Z. Zhang, *J. Mater. Chem. C*, 2018, **6**, 5375-5383.
- 37 J. Liu, L. Zhu, S. Xiang, Y. Wei, M. Xie, H. Liu, W. Li and H. Chen, *Sustain. Energy Fuels*, 2019, **3**, 184-194.
- 38 G. Gao, Q. Xi, H. Zhou, Y. Zhao, C. Wu, L. Wang, P. Guo and J. Xu, *Nanoscale*, 2017, **9**, 12032-12038.
- 39 L. Zhang, Q. Zeng and K. Wang, *J Phys Chem Lett*, 2017, **8**, 3752-3758.
- 40 X. Mo, X. Li, G. Dai, P. He, J. Sun, H. Huang and J. Yang, *Nanoscale*, 2019, **11**, 21386-21393.
- 41 D. M. Calistru, L. Mihut, S. Lefrant and I. Baltog, *J. Appl. Phys.*, 1997, **82**, 5391-5395.
- 42 H. J. Kong, D. H. Won, J. Kim and S. I. Woo, *Chem. Mater.*, 2016, **28**, 1318-1324.
- 43 I.-S. Cho, D. W. Kim, S. Lee, C. H. Kwak, S.-T. Bae, J. H. Noh, S. H. Yoon, H. S. Jung, D.-W. Kim and K. S. Hong, *Adv. Funct. Mater.*, 2008, **18**, 2154-2162.
- 44 S. K. Lakhera, H. Y. Hafeez, R. Venkataramana, P. Veluswamy, H. Choi and B. Neppolian, *Appl. Surf. Sci.*, 2019, **487**, 1289-1300.
- 45 J. Yu and A. Kudo, *Adv. Funct. Mater.*, 2006, **16**, 2163-2169.
- 46 C. Q. Li, X. Du, S. Jiang, Y. Liu, Z. L. Niu, Z. Y. Liu, S. S. Yi and X. Z. Yue, *Adv. Sci.*, 2022, **9**, e2201773.
- 47 J. Kou, C. Lu, J. Wang, Y. Chen, Z. Xu and R. S. Varma, *Chem. Rev.*, 2017, **117**, 1445-1514.
- 48 J. Wu, Y. Wang, S. Zhang, Y. Liu and F. Wang, *Appl. Catal., B*, 2023, **332**, 122741.
- 49 H. Han, X. Zheng, C. Qiao, Z. Xia, Q. Yang, L. Di, Y. Xing, G. Xie, C. Zhou, W. Wang and S. Chen, *ACS Catal.*, 2022, **12**, 10668-10679.
- 50 R. Yuan, S. Fan, H. Zhou, Z. Ding, S. Lin, Z. Li, Z. Zhang, C. Xu, L. Wu, X. Wang and X. Fu, *Angew. Chem. Int. Ed. Engl.*, 2013, **52**, 1035-1039.
- 51 W. Sheng, X. Wang, Y. Wang, S. Chen and X. Lang, *ACS Catal.*, 2022, **12**, 11078-11088.
- 52 X. Li, S. Lyu and X. Lang, *Environ. Res.*, 2021, **195**, 110851.
- 53 Z. Dong, Z. Zhang, Y. Jiang, Y. Chu and J. Xu, *Chem. Eng. J.*, 2022, **433**, 133762.
- 54 X. Li, S. Lu, J. Yi, L. Shen, Z. Chen, H. Xue, Q. Qian and M. Q. Yang, *ACS Appl. Mater. Interfaces*, 2022, **14**, 25297-25307.
- 55 W. Liao, W. Chen, S. Lu, S. Zhu, Y. Xia, L. Qi, M. Q. Yang and S. Liang, *ACS Appl. Mater. Interfaces*, 2021, **13**, 38239-38247.
- 56 T. Shan, L. Luo, T. Chen, L. Deng, M. Li, X. Yang, L. Shen and M.-Q. Yang, *Green Chem.*, 2023, **25**, 2745-2756.
- 57 M. Q. Yang, C. F. Tan, W. Lu, K. Zeng and G. W. Ho, *Adv. Funct. Mater.*, 2020, **30**, 2004460.
- 58 J. Wang, Z. Wang, J. Zhang, S. P. Chai, K. Dai and J. Low, *Nanoscale*, 2022, **14**, 18087-18093.
- 59 L. Liu, Z. Wang, J. Zhang, O. Ruzimuradov, K. Dai and J. Low, *Adv. Mater.*, 2023, DOI: 10.1002/adma.202300643, e2300643.
- 60 S. Lu, B. Weng, A. Chen, X. Li, H. Huang, X. Sun, W. Feng, Y. Lei, Q. Qian, M.-Q. Yang, *ACS Appl. Mater. Interfaces*, 2021, **13**, 13044-13054.
- 61 J. Wang, J. Li, W. Yang, Y. Liu, H. Wang, Q. Geng and F. Dong, *Appl. Catal., B*, 2021, **297**, 120489.
- 62 X. Zhao, B. Deng, F. Li, M. Huang, Y. Sun, J. Li and F. Dong, *J. Hazard. Mater.*, 2021, **420**, 126577.